Pressure-induced reentrant Dirac semimetallic phases in twisted bilayer graphene

Francisco Sánchez-Ochoa [1,*] Alberto Rubio-Ponce [2,†] and Florentino López-Urías [3,‡]

[1]*Departamento de Materia Condensada, Instituto de Física, Universidad Nacional Autónoma de México,*
Apartado Postal 20-364, Ciudad de México C.P. 01000, Mexico
[2]*Departamento de Ciencias Básicas, Universidad Autónoma Metropolitana-Azcapotzalco- Av. San Pablo 180,*
Ciudad de México C.P. 02200, Mexico
[3]*Advanced Materials Division, IPICYT, Camino a la Presa San José 2055, Col Lomas 4a sección, San Luis Potosí S.L.P., 78216, Mexico*

External hydrostatic pressure (P) is another controllable and clean knob to tune the energy position of van Hove singularities in twisted bilayer graphene (TBLG), besides the interlayer rotation angle (θ). Based on total energy density functional theory calculations, we report here the ground-state properties of high-angle TBLG with two families due to their even and odd sublattice-exchange parity, hereafter parity for simplicity, under vertical hydrostatic P. Even (odd) parity refers to rotate one layer with respect to the other in a bilayer graphene with stacking AA (AB). We observed a Dirac semimetal (0–20 GPa) semiconductor (20–70 GPa) phase transition at $\theta = 21.8°$ and $13.4°$; however, a reentrant Dirac semimetallic phase is observed for $\theta = 9.4°$ and $P \geqslant 70$ GPa whenever TBLG has even parity. Meanwhile, TBLG systems with odd parity and different θ remain metallic but with an enhanced trigonal warping for $P > 50$ GPa. Indeed, the semiconductor phase is only present for high θ. The phase transition in TBLG with even parity and the metallic character of TBLG with odd parity are due to band inversion effect assisted by a band-to-band repulsion mechanism shown by unfolded bands. This work shows the relevance of external P and parity in TBLG electronic structure and their possible implications in experiments.

I. INTRODUCTION

Twisted bilayer graphene (TBLG) system, also known as graphene moiré superlattice, is a new research platform to study exotic phases in condensed matter physics since the discovery of superconducting and Mott-insulator phases [1,2]. Since then, other interesting phenomena have been observed experimentally as electronic nematic phases [3], ferromagnetism near three-quarters filling [4], orbital magnets [5], the anomalous Hall effect [6], the light-induced Hall effect version [7], and intrinsic pseudomagnetic and potential fields [8], among others. Furthermore, theoretical reports predict on topological superconductivity [9], Wigner crystallization instead of Mott-insulating behavior [10], anisotropic quantum confinement with signatures of quantum dots at high energies [11], and the possibility of using to TBLG as an enantiose-lective chiral sensor [12,13] because of its chirality [14], to mention some recent studies.

Many of the observed and predicted above-mentioned phenomena are ascribed to "flat" bands close to the Fermi energy [15,16]. These flat bands are generated by the hybridization of Dirac cones in energy-momentum space; and the energy position of flat bands can be tuned by a simple twist between graphene layers. This in turn leads to van Hove singularities in the density of states and electron charge localization in regions

with AA stacking in real space forming a triangular pattern. Additionally, while the electronic charge density shows a C_6 symmetry in graphene monolayer, the charge density in TBLG with flat bands at the Fermi energy develops a C_3 symmetry. However, even when many experimental and theoretical reports have shown the TBLG properties to date, less attention has been paid to the importance of the parity (or translational offset), and θ on the electronic structure of TBLG aside from Mele [17,18]. Employing a continuum model, to mention the presence of a small band gap in TBLG has been confirmed if the parity is even [19]. Nevertheless, when TBLG is studied with different parity through tight-binding calculations, the small band gap for systems with even parity is not reported although the asymmetry is observed at low energies [20]. Khatibi *et al.* [21] studied the strain effect on commensurate TBLG systems with different sizes and thus parity. They found that the system with odd parity remains metallic but the band gap for the system with even parity increases when applying biaxial strain. Additionally, the tuning of the small band gap has been recently addressed [22] with different degrees of freedom as (again) the strain, electric fields and the interlayer distance emulating an external P but only for the first small commensurate TBLG of $\theta = 38.2°$, which is equivalent to $\theta = 21.8°$ by symmetry.

Here, it is worth to mention that the interlayer distance (d) in twisted systems is now also considered another knob for tuning the electronic properties [23,24]. In fact, d which can be parametrized in terms of an external P, is equiva-lent to θ [$P(d) \propto \theta$] in TBLG, to observe superconductivity [25], flat bands at low energy in theory [26–28], or develop

*fsanchez@fisica.unam.mx
†arp@azc.uam.mx
‡flo@ipicyt.edu.mx

half-metallicity and magnetism [29,30] with supercells having smaller moiré patterns than that with the "magic angle" $\theta = 1.08°$ [1]. Therefore, P is a controllable alternative way to modulate the TBLG electronic and magnetic properties within the standard density functional theory (DFT) framework, including many-body effects [31], because twisted systems could have less atoms. Although many reports have contributed to the field of moiré physics addressing the hydrostatic pressure role, there are still some questions to figure out regarding the interplay among P, θ, and the initial parity.

Accordingly, in this study, we report results of theoretical studies on the parity in TBLG under hydrostatic P. First, we used DFT calculations to estimate the external P as a function of compression ε from bulk graphite and bulk TBLG systems with three different θ and even and odd parities. Then, we calculate the ground state of each TBLG as slab taking into account in-plane relaxation of atomic positions with fixed d. In addition, we used an unfolding method [32] to obtain an effective band structure which could be comparable to angle-resolved photoelectron spectroscopy (ARPES) measurements to show clearly the mechanism of band-to-band repulsion present. As we shall see, an interesting result is that TBLG can undergo semimetallic-semiconductor-semimetallic phase transitions whether TBLG has even parity, conversely TBLG with odd parity has metallic behavior with enhanced trigonal warping at high P.

II. COMPUTATIONAL METHODOLOGY

Total energy DFT calculations were performed using the SIESTA package [33,34]. The Perdew-Burke-Ernzerhof (PBE) parametrization within the generalized gradient approximation (GGA) for exchange-correlation effects was used [35], while the electron-ion interactions are treated with norm-conserving pseudopotentials [36]. As SIESTA uses a linear combination of numerical pseudoatomic orbitals (LCAO), here we employed an optimized single-ζ polarized (SZP) basis set to expand the Khon-Sham wave functions and an energy mesh cutoff of 350 Ry for sampling the electronic density in the real space. Structural parameters and forces were well converged using a Γ-centered $63 \times 63 \times 9$ Monkhorst-Pack k grid [37] for the smallest bulk TBLG ($\theta = 21.8°$) while for TBLG as slab the k grid was $63 \times 63 \times 1$. An electronic temperature of 10 K was used for the Fermi surface broadening. The optimization of atomic positions and lattice vectors was performed until residual forces were 5 meV/Å or less, and the threshold value for electronic self-consistency was set to 10^{-4} eV. To simulate TBLG as slab, we employ the supercell (SC) method with a vacuum space of 20 Å between adjacent graphene monolayers to avoid artificial interactions. Visualization of atomic models is performed using the VESTA program [38].

Commensurate TBLG systems were built following the procedure in Refs. [11,32], for $\theta = 21.8°$, $13.2°$, and $9.4°$ with different initial even and odd parities as shown in Figs. 1(a) and 1(b), respectively. Notice that the two structures have the same number of carbon atoms inside the SC, however, the even parity has a C_6 symmetry and the system with odd parity has a lower C_3 symmetry.
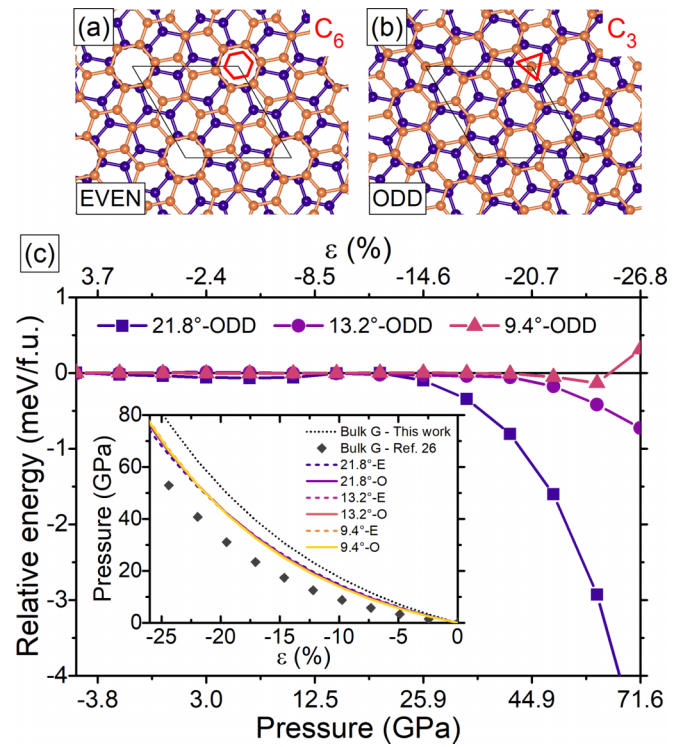

FIG. 1. Top view of TBLG with $\theta = 21.8°$ and (a) even parity and (b) odd parity. The black line encloses the periodic supercell. Red hexagon depicts the C_6 symmetry centered in a hollow position in (a) while the red triangle is for top position in (b) having a C_3 symmetry. Blue and orange spheres represent carbon atoms at the bottom and top graphene monolayer, respectively. (c) Relative energy between optimized TBLGs with even parity and odd parity as a function of P and/or ε. The TBLG systems with even parity were taken as reference with zero energy. The inset shows the relationship between P and ε for different bulk TBLGs system in comparison with the calculated data for bulk graphite in this work (bulk G: this work) and with data from Ref. [26] (bulk G: Ref. [26]). The relative energy is in meV per formula unit (f.u.) of graphene.

III. RESULTS AND DISCUSSION

A. Pressure and atomic reconstruction

We first discuss the optimized crystal structures of bulk graphite, and bulk TBLG which can be considered as a periodic system of alternatively twisted graphene monolayers [39]. At ambient pressure (0 GPa), the optimizing process of atomic positions and lattice vectors for every system in bulk gives a V_0 reported in Table I. This V_0 value is in principle comparable to experimental results but different from other theoretical reports due to computational methodology. Once the volume parameters were determined, we took the optimized positions of C atoms and fix the lattice vectors. Then, the magnitude of c vector was decreased to simulate an external hydrostatic pressure as first approximation by replicas of graphene layers in neighbor SCs. Thus, d was mapped to $\varepsilon = 1 - d/d_0$, such that ε was varied from 0% to ~25% with $d_0 = 3.12$ Å for bulk graphite and $d_0 = 3.20$ Å for bulk TBLG systems. Different values of ε lead also to different values of V and E correspondingly. The calculated energy-volume data

TABLE I. Optimized values of equilibrium volume V_0, bulk modulus B_0, and its derivative B_0'. A and β are parameters for the Eq. (3). P_{max} is the maximum pressure loaded in bulk TBLG (3D) and as slab (2D) with different parity. $|$ Max Δ $|$ represents the modulus of the maximum displacement vector Δ for carbon atoms.

| System | Graphite | 21.8° | | 13.2° | | 9.4° | | | Graphite | |
parity	Odd	Even	Odd	Even	Odd	Even	Odd	Odd[a]	Odd[b]	Odd[c]
V_0 (Å³/atom)	8.34	8.49	8.50	8.55	8.53	8.55	8.55	5.24	11.36	5.04
B_0 (GPa)	117.93	113.22	106.64	95.11	98.15	93.12	93.48	15.50	33.80	
B_0'	5.23	4.71	5.16	5.62	5.51	5.78	5.73	13.60	8.90	
A (GPa)	17.87	15.32	13.53	12.37	12.66	11.91	11.97			5.73
β	6.83	6.77	7.26	7.58	7.50	7.74	7.71			9.54
P_{max}(3D) (GPa)	67.76	70.84	71.27	71.23	70.86	72.36	71.79			
P_{max}(2D) (GPa)		68.02	69.55	69.98	69.94	70.65	70.31			
$|$ Max Δ $|$ (mÅ)	0.00	6.80	8.44	16.82	21.17	40.31	39.56			

[a]Theoretical data from Ref. [31].
[b]Experimental data from Ref. [43].
[c]Theoretical data from Ref. [26].

sets were fitted using the Murnaghan equation of state [40]:

$$E(V) = E(V_0) + \frac{B_0 V}{B_0'}\left(\frac{(V_0/V)^{B_0'}}{B_0' - 1} + 1\right) - \frac{B_0 V_0}{B_0' - 1}, \quad (1)$$

where B_0 is bulk modulus at equilibrium volume V_0 and the bulk modulus derivative B_0'. Thus, one obtains $E_0 = E(V_0)$ at equilibrium energy. $P - V$ curves were then calculated as $P = dE/dV$ for every system from DFT calculations as follows:

$$P_{\text{DFT}}(V) = \frac{B_0 V}{B_0'}\left[\frac{1 - (V_0/V)^{B_0'}}{B_0' - 1}\right]. \quad (2)$$

Table I shows higher B_0 values and lower B_0' values when we compare with other reports. This large deviation in mechanical properties can be attributed to methodology (see Appendix). An interesting thing here is that, even when B_0 and B_0' are different, the B_0 value in this paper is greater than those for bulk TBLG. Large differences in B_0 and B_0' can be observed for bulk TBLG with $\theta = 21.8°$ and different parity, which means different mechanical properties for higher θ, although this difference is smaller for lower angles. After that, we now fitted the previously found $P_{\text{DFT}}(V)$ values to next function in terms of ε [26]:

$$P_{\text{FIT}}(\varepsilon) = A(e^{-\beta\varepsilon} - 1). \quad (3)$$

A and β values obtained with Eq. (3) and reported in Table I are different from those found in Ref. [26] and frequently used in other reports [41,42]. The inset in Fig. 1(c) shows the results of $P_{\text{FIT}}(\varepsilon)$ plot using Eq. (3) for every bulk TBLG system (with different parity) in comparison with bulk graphite and with the data from Ref. [26]. As shown in inset of Fig. 1(c), the data of $P_{\text{FIT}}(\varepsilon)$ function follow the Eq. (2) with $\sim$80 GPa and $\sim$70 GPa for bulk graphite and bulk TBLG, respectively, for $\varepsilon \simeq 25\%$. This interesting result clearly shows that the loaded pressure on TBLG systems is lower than bulk graphite for high ε. Additionally, the relative energy between even parity and odd parity as a function of P or ε is large for $\theta = 21.8°$. Such relative energy is small for low θ, but indeed the even-parity configuration is more stable than odd parity at high pressure. We know that our theoretical predictions of $P(\varepsilon)$ are overestimated in comparison with those in Ref. [26], however,

it is noteworthy to mention that these values are more reliable than those in Ref. [30] with similar methodology and only even parity, or in Ref. [28] with DFT and plane-wave calculations and only odd parity. Atomic reconstructions in TBLG can change the electronic properties at low energy because of the size imbalance between AB- (BA-) and AA-stacking regions in moiré patches, especially at low [44,45] or marginal θs [8,46–49]. Here, we have kept the atoms free to relax along x and y directions at different P while the z coordinate was fixed. Carbon atoms shift from initial position around the C_6 and C_3 rotation axes with different size, hereafter Δ, if the initial parity is even or odd. Figures 2(a) and 2(b) show atomic displacement fields (or atomic reconstructions) with an anticlockwise sense for graphene bottom layers having $\theta = 9.4°$, while those graphene layers on top have clockwise direction. $\Delta = 20$ mÅ is the maximum value found in this case when $P = 34$ GPa. Table I and Fig. 2(c) report the maximum absolute value of Δ for three different high angles with even parity and odd parity as a function of P, as well as the maximum value of P when the TBLG systems are considered as bulk [three dimensional (3D)] or slabs [two dimensional (2D)]. The atomic reconstruction in these systems can be ascribed to screw dislocations, but more important is that the possible implications of these strain fields are in the generation of pseudoscalar (V_{pse}) and vector (B_{pse}) potentials [50,51] and of course pseudo-Landau levels [8]. The quantification of V_{pse} and B_{pse} is an interesting topic that we will address in the future. To end this subsection let us mention that previous theoretical reports have disregarded this strain effect [29,30] which probably could suppress the ferromagnetism localized in AA regions at lower θ.

B. Electronic structure and phase transition

Figure 3 shows the TBLG electronic properties for $\theta = 21.8°$ around the Fermi energy, with different parity and pressure. Now we discuss the electronic properties of TBLG with even-parity. From Fig. 3(a), we can see first the well-known energy tendency of van Hove singularities (VHSs) approaching the Fermi energy (0 eV) as P increases. The first set of VHSs, generated due to π-band hybridization in valence and conduction regimes between two graphene layers, are denoted
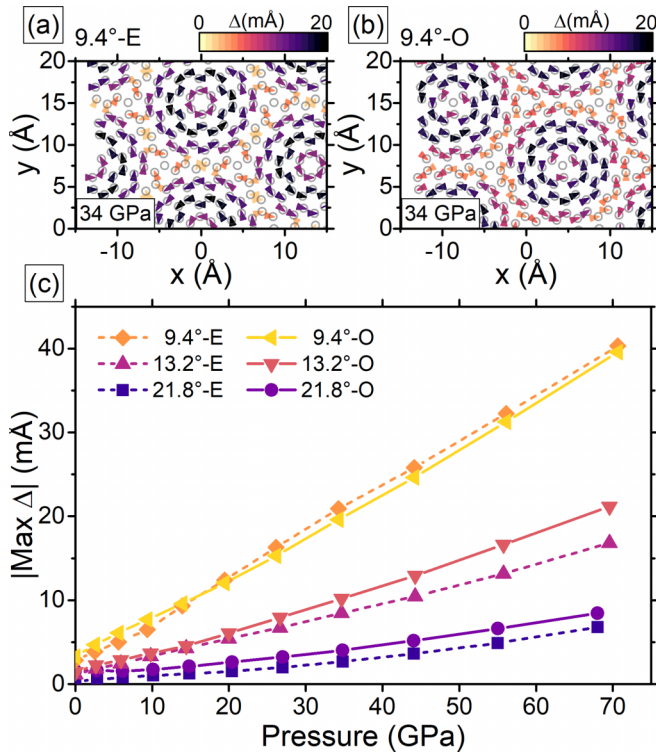
FIG. 2. (a), (b) Show atomic displacement fields of carbon atoms in the bottom layer with different even (E) or odd (O) parity, and high P. Empty gray circles represent the initial atomic positions and arrowheads shows the direction and the size of atomic displacement Δ. (c) Modulus of maximum Δ as a function of P for different values of θ and parity.

as VHS1 in Fig. 3(a). In the same figure, the Dirac point (DP) is identified as narrow dark energy region for $P < 20$ GPa, nevertheless, for $P \geqslant 20$ GPa, the system undergoes a semiconductor phase transition. The size of this narrow band gap can be tuned by pressure with a maximum value achieved of 78 meV at 43 GPa. In addition, a second set of VHSs (VHS2) is observed at high P due to an energy band splitting of VHS1. The energy separation between VHS1 and VHS2 at high pressure is $\simeq 1$ eV in valence and $\simeq 0.75$ eV in conduction regimes due to electron-hole asymmetry. A third set of VHSs (VHS3) is further observed below -1 eV. These results are in fair agreement with other reports based on DFT [21,22] and tight binding [17] where the appearance of electronic band gap is owing to even parity of TBLG. On the other hand, the electronic structure of TBLG with odd parity in Fig. 3(d) is similar to that with even parity in Fig. 3(a) for $P < 20$ GPa, but for $P \geqslant 20$ GPa the electronic structure is fully different since (1) the system is now metallic, (2) the VHS1 set does not arrive the Fermi energy symmetrically; only the VHS1 in valence is closer to Fermi energy than that VHS1 in conduction regime, (3) VHS2 and VHS3 are nearer to 0 eV in comparison with the system of even parity plus an energy difference >0.5 eV as well. This metallic character found here is consistent with previous report [28] where the authors studied several TBLG systems with only odd parity at high P. This is because their reported band structure with $\theta = 21.8°$ is similar to that in Fig. 3(e).

Four representative TBLG systems were taken into account to show differences at high P and parity. The electronic band structure and DOS with even parity are plotted in Figs. 3(b) and 3(c), respectively, while Figs. 3(e) and 3(f) are the corresponding for TBLG with odd parity. In general, the band structures at ~ 68 GPa are different due to initial parity in TBLG. While systems with even parity are semiconducting, the systems with odd parity are metallic. Note that the parity in TBLG is like pseudo-spin-orbit coupling breaking time-reversal and inversion symmetries [52,53]. Accordingly, the band splitting observed in Fig. 3(b) is Rashba-type spin-orbit coupling (inversion-symmetry breaking) and Fig. 3(e) develops a Zeeman-type band splitting (time-reversal symmetry breaking) [17]. As shown, the band splitting in momentum or energy decreases as the P does. Figures 3(c) and 3(f) show the DOS for every parity where in both cases the VHSs tend to the Fermi energy but they never overlap for even parity because of the band-gap formation; meanwhile those VHSs for odd-parity system are far away from Fermi energy although a sudden falling of DOS just at the Fermi energy and an increase at 0.12 eV for $P = 65$ GPa could be ascribed to the edges of a pseudo-band gap. This is because some bands cross the Fermi energy between these edges and the nonzero DOS. Until here, we have identified a Dirac semimetal-narrow band-gap semiconductor phase transition for $P > 20$ GPa in agreement with previous reports [21,22].

The effect of moiré supercell size on electronic properties is now discussed. Figures 4(a) and 4(d) show the color-map plots of DOS in logarithm scale for next commensurate lower angle $\theta = 13.2°$ at different P and parity. Again, the general trend of VHSs approaching the Fermi energy is observed. The two systems have a Dirac point at the Fermi energy for $P < 20$ GPa where the energy position of VHSs in both valence and conduction regimes, with respect to Fermi energy, is lower as θ decreases. This is a well-known effect due to reduction of separation distance between neighbor Dirac cones in momentum space. Second, VHSs approach faster the Fermi energy whether θ is lower and P is higher, in particular, if TBLG systems have even parity as shown here. The energy separation between consecutive VHSs (in valence and conduction regimes) tends to decrease as θ also does, but more important is the fact that this energy difference depends on the initial parity. From these results, we can conclude that (1) TBLG systems with odd parity have metallic character, (2) conversely TBLG with even parity have a tunable narrow band gap in terms of θ, P, and of course stacking.

Now we plot in Figs. 4(b) and 4(e) the band structures and their corresponding DOS in Figs. 4(c) and 4(f) for four high pressures in a small energy window around the Fermi energy. Notice that the systems with $\theta = 13.2°$ and even parity are semimetallic for $P = 26$ GPa and semiconducting when $P = 44$ GPa. If the system has $\theta = 13.2°$ the semiconductor behavior remains [see Fig. 4(b)]. TBLG with odd parity always remains metallic with a pseudogap above the Fermi energy tunable by pressure and θ. It is noteworthy to mention that the energy position of Fermi energy can be tuned in experiments to move it inside the pseudogap which can transform the system to a "poor metal." Another pseudogap of ~ 0.22 eV can be identified from -0.38 to -0.16 eV when the parity is odd [see Fig. 4(f)]. Notice that a couple of van Hove singularities can
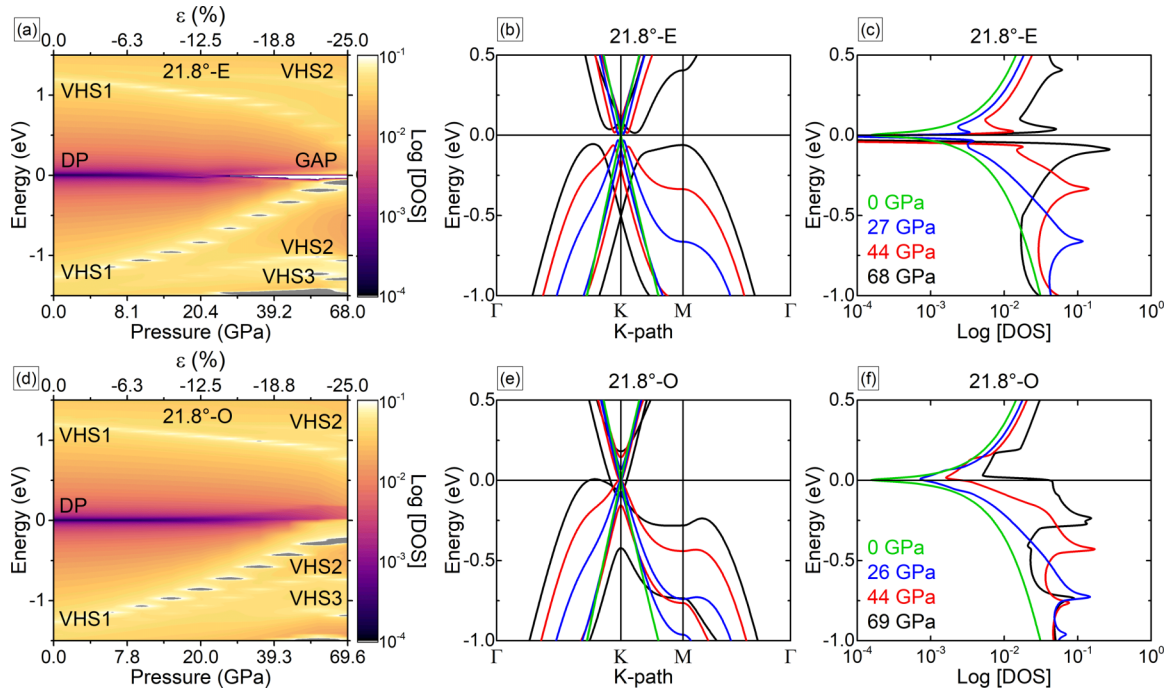
FIG. 3. (a,) (d) Show the logarithm scale density of states (DOS) as a function of energy, pressure, and compression for TBLG with $\theta = 21.8°$ and different parity, even (E) and odd (O). (b), (c) Show the band structure and their corresponding DOS of TBLG, respectively, with even parity at four different pressures. (e), (f) Plots represent the same as (b) and (c) but for odd parity. Dirac point (DP), first (VHS1), second (VHS2), and third (VHS3) van Hove singularities and band gap (GAP) can be identified in (a) and (d). The Fermi level is set at 0 eV.

be observed in conduction regime which energy difference is smaller when the initial parity is odd.

However, on one hand the TBLG system is semimetallic for $\theta = 9.4°$, even parity, and $P = 70$ GPa, showing a Dirac cone along the Γ-M k path of Brillouin zone supercell [see green circle in Fig. 5(b)]. On the other hand, the TBLG with

the same θ and P but with odd parity now shows a Dirac cone along the Γ-K k path of Brillouin zone [see green circle in Fig. 5(e)]. The energy difference between VHS1 and VHS2 in conduction regimes reduces as θ decreases. For odd parity and $\theta = 9.4°$, the pseudogap positioned in -0.20 eV also reduces its size to ∼0.18 eV [see Fig. 5(f)]. Therefore, we

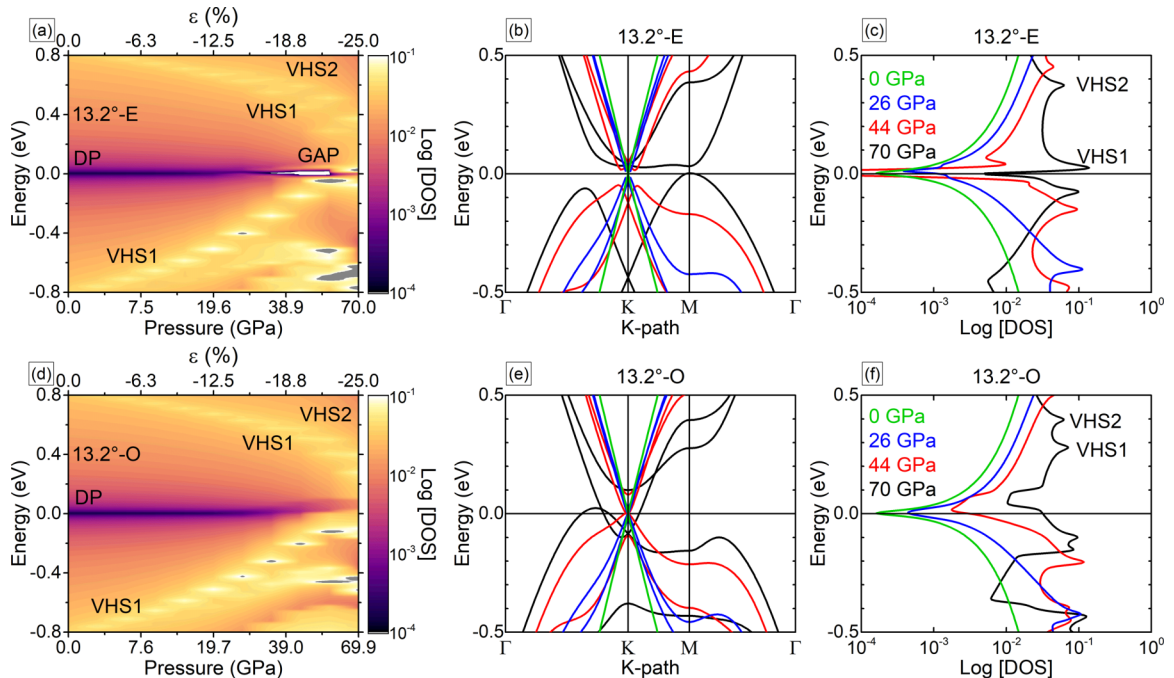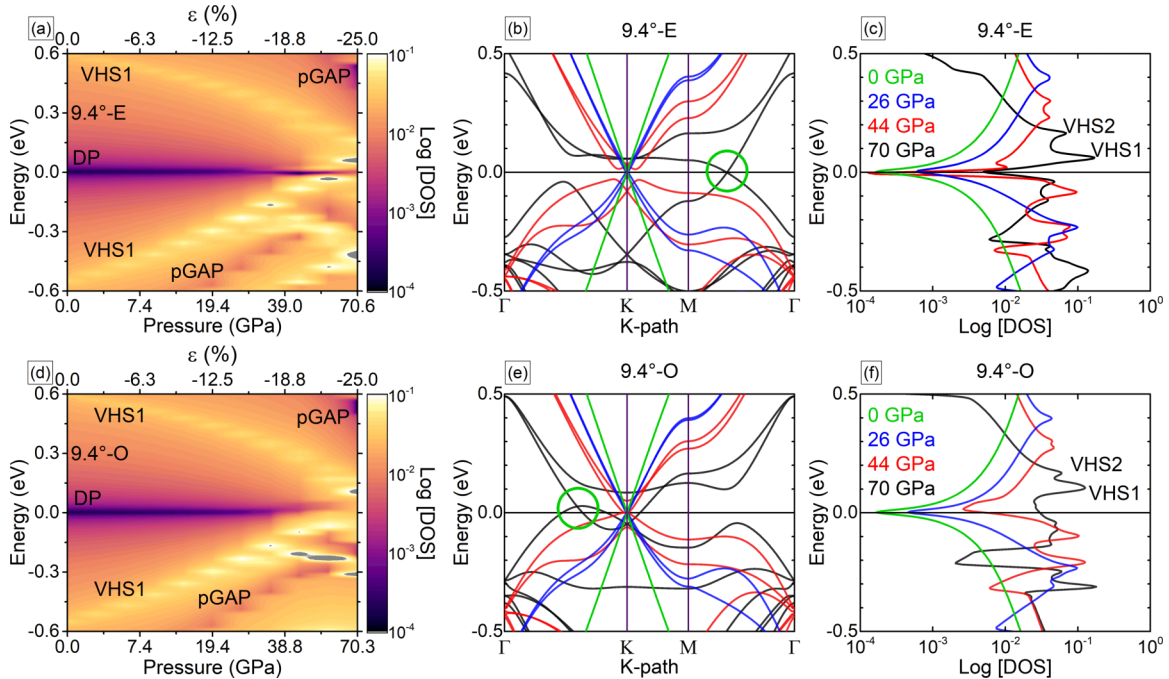FIG. 4. The same as in Fig. 3 but now for $\theta = 13.2°$ with different parity, even (E) and odd (O).

FIG. 5. The same as in Fig. 3 but now for $\theta = 9.4°$ with different parity, even (E) and odd (O). Additionally, pseudogaps (pGAPs) can be identified. Green circles show Dirac cones.

have observed a reentrant Dirac semimetallic phase for TBLG systems with low θ and even parity under high pressure not reported yet. The Dirac cone is confined to Γ-M path if TBLG has even parity [see Fig. 5(b)]. For the same θ but odd parity, the Dirac cone is now positioned along the Γ-K path [see Fig. 5(e)] plus a Dirac cone positioned at the K point. These emergent Dirac cones along these high-symmetric k paths in supercell reciprocal space can be attributed to parity [17,18], with C_6 or C_3 symmetry.

Figure 6 shows the density plot around the Fermi energy for the valence band maximum (VBM) and conduction band minimum (CBM) of TBLG with even and odd parity for $\theta = 9.4°$ and 70 GPa. Figures 6(a) and 6(b) clearly show the generation of Dirac cones as well as Dirac points touching at zero eV along the Γ-M k path instead of the corner of supercell Brillouin zone. On the other hand, TBLG with odd parity [Figs. 6(c) and 6(d)] develops an enhanced trigonal warping effect because the parabolic dispersion at the Dirac point splits into four Dirac cones with linear dispersion [54,55] reflecting the threefold in-plane rotational symmetry. This trigonal warping effect is due to an enhancement of interlayer tunneling between nondimer sites as the interlayer distance decreases, i.e., third-nearest-neighbor hopping interactions matter. The primary Dirac cones are located at the corner of the Brillouin zones, while the other three are shifted from the corner towards the Γ point along the Γ-K k path. Notice that while these so-called "satellite" Dirac points are located along the K-K' in bulk graphite ($\theta = 60°$), here they are positioned along the Γ-$K(K')$ k path. These results are in agreement with previous reports for TBLG under in-plane tensile strain [21] or with $\theta < 1.06°$ as in Ref. [2]. Another important aspect to mention is that the associated Lifshitz transition, related to the trigonal warping, would be connected with conservation of topological charge as in bilayer graphene

[56] or in TBLG with low θ [2]. Topological charges as well as entanglement [57] are interesting topics to explore in these graphene systems at high pressure.
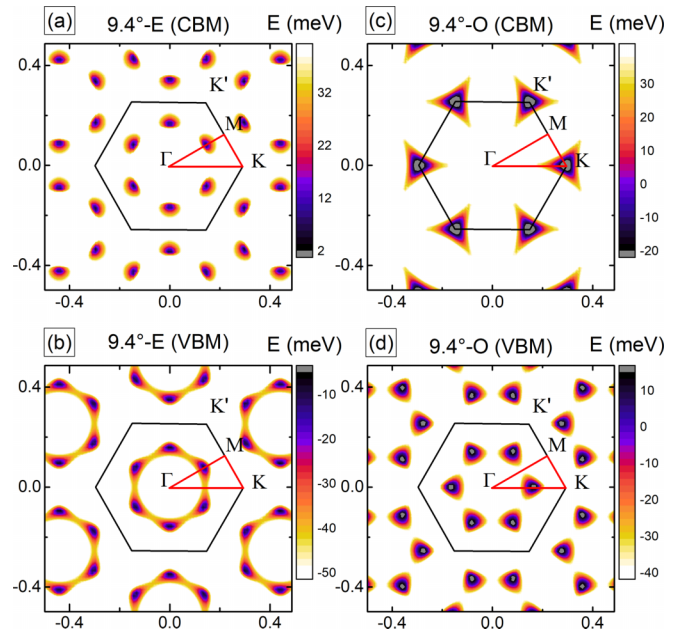

FIG. 6. Contour plots of eigenvalue states as a function of k_x and k_y in momentum space for $\theta = 9.4°$ with different parity, even (E) and odd (O), and $P = 70$ GPa for the valence band maximum (VBM) and conduction band minimum (CBM). The first Brillouin zone edges are marked by the black hexagon while irreducible Brillouin zone is delimited by red triangle with high-symmetry points. k_x and k_y are in Å^{-1}.

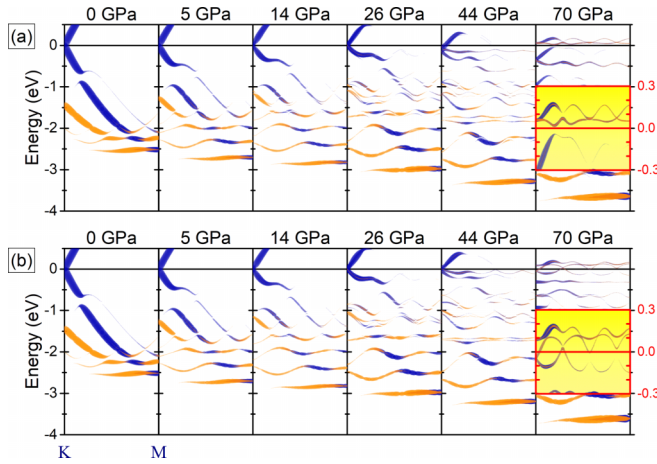FIG. 7. Effective band structures calculated through the unfolding approach for $\theta = 9.4°$ with (a) even parity and (a) odd parity at different pressures. The unfolding was performed onto the K-M k path of the graphene primitive cell in blue, where TBLG supercell states are projected onto both graphene primitive cells. The top (bottom) graphene layer is highlighted with blue (orange) lines, where the width of the lines is proportional to spectral weight, $W(k, I)$. The line widths are scaled $\times 1$, $\times 1$, $\times 1.5$, $\times 1.5$, and $\times 2.5$ for $P = 5, 14, 26, 44$, and 70 GPa, respectively, with respect to the line width at 0 GPa. The line width in red insets with yellow background are scaled $\times 4$ as well. The Fermi energy is set to 0 eV.

C. Unfolding and band repulsion

The "folding" of electronic bands is a common issue in solid-state physics for periodic systems with many primitive cells forming a TBLG. This problem gives a bunch of electronic states collapsed into supercell Brillion zone which is smaller than the original graphene primitive cell. This folding mechanism sometimes gives a difficult or otherwise impossible interpretation of physical interactions in a wide energy range. The previous discussion of results is a clear example of the problem stated before. Additionally, a standard supercell band structure calculation does not have a direct comparison with ARPES measurements. Hence, an unfolding (inverse) approach can solve this problem to obtain an effective band structure showing electronic interactions which we can compare with experimental data. Now, we move on with a more detailed discussion on the unfolded electronic band structure of TBLG systems, with different parity and P for $\theta = 9.4°$, in a wide energy range around the Fermi energy and along the K-M path of blue graphene primitive cell, which is the bottom graphene layer in Fig. 1. The selection of this k path is because major changes in band structure of graphene primitive cell are observed along this k path [11]. The spectral weight, $W(k, I)$, calculations were performed to distinguish those TBLG supercell electronic states having the same symmetry as those of graphene primitive cell of reference. Along the same k path, we also projected the TBLG states of orange graphene primitive cell, which is the top graphene layer in Fig. 1 [11,32].

As can be seen in Fig. 7 for 0 GPa, both even and odd parities have a similar band structure. In this case the observed discontinuities in blue bands above -1 eV are due to band hybridization between two TBLG systems giving an energy

gap between K_{blue}-K_{orange}. This in turn, originates VHSs in the DOS which are tunable in energy by θ, or P as shown in this paper. In addition, the set of less dispersive flat bands composed of both graphene layers states is reproduced for energies below of -2 eV. It is worth to mention that the presence of high-energy Dirac cones near the M point at -2 eV is confirmed. For higher pressures, the electronic structure changes and it must show large differences between even and odd parities. The common feature between Figs. 7(a) and 7(b) from 5 to 26 GPa is the increasing band-gap size above -1 eV near the K point. This trend is difficult to observe and follow at higher pressures. However, the energy difference between consecutive flat bands at high energy in valence regime has the same behavior as the aforementioned band gap near the K point, i.e., the energy separation increases as the pressure does resembling a band-to-band repulsion mechanism. This band repulsion mechanism can be considered as the main effect to move the VHSs energy position towards the Fermi energy. In addition, we mention that for $P = 44$ GPa, the band structure shows a band splitting near the K point close to Fermi energy in comparison with the band structure at $P = 26$ GPa. The last band structure at $P = 70$ GPa is very different to those for $P < 26$ GPa, although it is possible to observe that the energy-band splitting is enhanced for bands below the Fermi energy close to K point for both parities going from $P = 44$ to 70 GPa. This effect can be interpreted as a band-inversion mechanism. The red insets with yellow background for these systems are zoomed-in views along the full K-M path and around the Fermi energy. Note that the band structure for TBLG with even parity does not show a Dirac cone along the scanned k path, if we compare this result with supercell band structure in Fig. 5(b). This apparent semiconductor behavior must be due to the scanned k path connecting the K and M points of graphene primitive cell. On the other hand, the band structure of TBLG with odd parity shows clearly the primary (electron-doped) Dirac cone together with a (hole-doped) satellite Dirac cone crossing the Fermi level. This last result agrees with the supercell band structure plotted in Fig. 5(e), but more important is the fact that this result could be compared with ARPES measurements.

To end, let us mention that this is a theoretical prediction of reentrant Dirac semimetallic phase in TBLG under hydrostatic pressure. At specific compression, our calculated pressure is overestimated in comparison with other theoretical reports for bulk graphite [26]; however, this result suggests that our predicted pressures for TBLG should be lower than bulk graphite to observe phase transitions (see inset of Fig. 1). For example, with $\varepsilon = -25\%$ we calculate $P = 70.55$ GPa for TBLG with $\theta = 9.4°$ and even parity, $P = 80.68$ GPa for bulk graphite with our methodology, and $P = 56.49$ GPa for bulk graphite with data from Ref. [26]. This leads to a ratio of $70.55/80.65 = 0.87$ between the first two pressures, and thus the expected value for TBLG with plane waves would be $0.87 \times 56.49 = 49.14$ GPa. This $P = 49.14$ GPa is greater than 20 GPa (as in recent experiment [58]) but more reliable than 70 GPa. We expect that TBLG with lower θ shows these reentrant Dirac semimetallic phases at lower pressure but indeed in a wide range of pressure accessible for experiments with diamond anvil cells [58]. We further have shown that the initial parity could be an important factor in experiments. Last
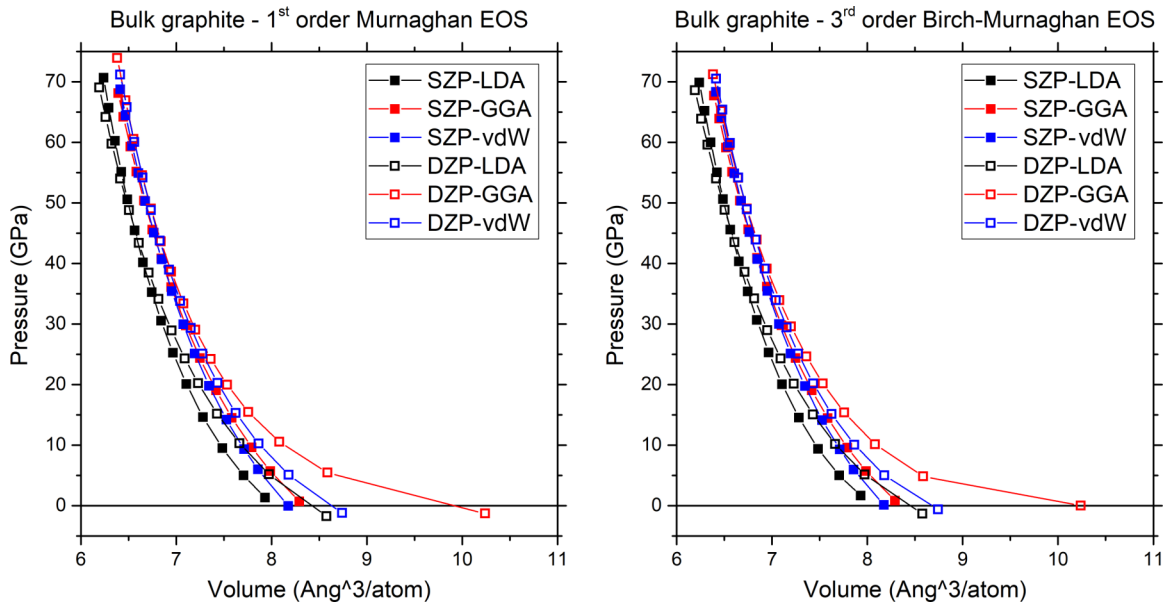
FIG. 8. P vs atomic volume data for bulk graphite employing different equations of states (EOSs) for several basis-set sizes and exchange-correlation functionals, as local density approximation (LDA), generalized gradient approximation (GGA), and van der Waals (vdW).

but not least, this system under high pressure could transform into 2D diamond as well, termed as moiré diamones, which deserve further studies [59–61].

IV. CONCLUSIONS

In summary, we have presented a detailed and systematic study of the electronic structure of TBLG using DFT. The interplay among twist, pressure, and parity for tuning the electronic structure was discussed. We found that the external pressure can be lower for TBLG systems in bulk when comparing with the bulk graphite as well; and the calculated pressure can be indeed lower in experiments because the overestimated values in comparison with other plane-wave methodologies. Most interesting is our finding that a reentrant Dirac semimetallic phase is observed for lower angles and high pressure after an intermediate narrow semiconducting phase whenever TBLG has even parity, whereas that TBLG with initial odd parity remains metallic with an enhanced trigonal warping mechanism. This trigonal warping gives four Dirac cones with different topological charge. Our results demonstrate the relevance of initial parity on electronic properties of pressurized moiré graphene superlattices that should be relevant in experiments.

APPENDIX: EQUATION OF STATES

We have tested with a third-order equation of state (EOS) of Birch [62] and Murnaghan to obtain bulk modulus, its second derivative, and the pressure vs volume relationship and then compare these results with those of first-order Murnaghan EOS [40]. The results with SZP and DZP show almost the same numerical values for mechanical properties with GGA(PBE); however, the lack of good description in comparison with experimental results is ascribed to exchange-correlation functional as well as the basis-set size used. Figure 8 shows that different exchange-correlation functionals lead to the same values of P per atomic volume. From this analysis we adopted the SZP-GGA as the optimal approach to study bulk graphite and hence the TBLG systems.

[1] Y. Cao, V. Fatemi, S. Fang, K. Watanabe, T. Taniguchi, E. Kaxiras, and P. Jarillo-Herrero, Unconventional superconductivity in magic-angle graphene superlattices, Nature (London) **556**, 43 (2018).

[2] Y. Cao, V. Fatemi, A. Demir, S. Fang, S. L. Tomarken, J. Y. Luo, J. D. Sánchez-Yamagishi, K. Watanabe, T. Taniguchi, E. Kaxiras *et al.*, Correlated insulator behaviour at half-filling in magic-angle graphene superlattices, Nature (London) **556**, 80 (2018).

[3] Y. Cao, D. Rodan-Legrain, J. M. Park, N. F. Yuan, K. Watanabe, T. Taniguchi, R. M. Fernandes, L. Fu, and P. Jarillo-Herrero, Nematicity and competing orders in superconducting magic-angle graphene, Science **372**, 264 (2021).

[4] A. L. Sharpe, E. J. Fox, A. W. Barnard, J. Finney, K. Watanabe, T. Taniguchi, M. Kastner, and D. Goldhaber-Gordon, Emergent ferromagnetism near three-quarters filling in twisted bilayer graphene, Science **365**, 605 (2019).

[5] X. Lu, P. Stepanov, W. Yang, M. Xie, M. A. Aamir, I. Das, C. Urgell, K. Watanabe, T. Taniguchi, G. Zhang *et al.*, Superconductors, orbital magnets and correlated states in magic-angle bilayer graphene, Nature (London) **574**, 653 (2019).

[6] M. Serlin, C. Tschirhart, H. Polshyn, Y. Zhang, J. Zhu, K. Watanabe, T. Taniguchi, L. Balents, and A. Young, Intrinsic quantized anomalous hall effect in a moiré heterostructure, Science **367**, 900 (2020).

[7] J. W. McIver, B. Schulte, F.-U. Stein, T. Matsuyama, G. Jotzu, G. Meier, and A. Cavalleri, Light-induced anomalous hall effect in graphene, Nat. Phys. **16**, 38 (2020).

[8] H. Shi, Z. Zhan, Z. Qi, K. Huang, E. v. Veen, J. Á. Silva-Guillén, R. Zhang, P. Li, K. Xie, H. Ji *et al.*, Large-area, periodic, and tunable intrinsic pseudo-magnetic fields in low-angle twisted bilayer graphene, Nat. Commun. **11**, 1 (2020).

[9] C. Xu and L. Balents, Topological Superconductivity in Twisted Multilayer Graphene, Phys. Rev. Lett. **121**, 087001 (2018).

[10] B. Padhi, C. Setty, and P. W. Phillips, Doped twisted bilayer graphene near magic angles: Proximity to wigner crystallization, not Mott insulation, Nano Lett. **18**, 6175 (2018).

[11] F. Sánchez-Ochoa, A. R. Botello-Méndez, and C. Noguez, Angle-dependent electron confinement in graphene moiré superlattices, Phys. Rev. B **104**, 075430 (2021).

[12] F. Hidalgo, A. Rubio-Ponce, and C. Noguez, Cysteine adsorption on twisted-bilayer graphene, J. Phys. Chem. C **125**, 27314 (2021).

[13] F. Hidalgo, A. Rubio-Ponce, and C. Noguez, Tuning adsorption of methylamine and methanethiol on twisted-bilayer graphene, J. Phys. Chem. C **123**, 15273 (2019).

[14] C.-J. Kim, A. Sánchez-Castillo, Z. Ziegler, Y. Ogawa, C. Noguez, and J. Park, Chiral atomically thin films, Nat. Nanotechnol. **11**, 520 (2016).

[15] M. Utama, R. J. Koch, K. Lee, N. Leconte, H. Li, S. Zhao, L. Jiang, J. Zhu, K. Watanabe, T. Taniguchi *et al.*, Visualization of the flat electronic band in twisted bilayer graphene near the magic angle twist, Nat. Phys. **17**, 184 (2021).

[16] S. Lisi, X. Lu, T. Benschop, T. A. de Jong, P. Stepanov, J. R. Duran, F. Margot, I. Cucchi, E. Cappelli, A. Hunter *et al.*, Observation of flat bands in twisted bilayer graphene, Nat. Phys. **17**, 189 (2021).

[17] E. J. Mele, Commensuration and interlayer coherence in twisted bilayer graphene, Phys. Rev. B **81**, 161405 (2010).

[18] E. Mele, Interlayer coupling in rotationally faulted multilayer graphenes, J. Phys. D: Appl. Phys. **45**, 154004 (2012).

[19] J. L. Dos Santos, N. Peres, and A. C. Neto, Continuum model of the twisted graphene bilayer, Phys. Rev. B **86**, 155449 (2012).

[20] P. Moon, Y.-W. Son, and M. Koshino, Optical absorption of twisted bilayer graphene with interlayer potential asymmetry, Phys. Rev. B **90**, 155427 (2014).

[21] Z. Khatibi, A. Namiranian, and F. Parhizgar, Strain impacts on commensurate bilayer graphene superlattices: Distorted trigonal warping, emergence of bandgap and direct-indirect bandgap transition, Diam. Relat. Mater. **92**, 228 (2019).

[22] X.-C. Jiang, Y.-Y. Zhao, and Y.-Z. Zhang, Tunable band gap in twisted bilayer graphene, Phys. Rev. B **105**, 115106 (2022).

[23] M. Yankowitz, J. Jung, E. Laksono, N. Leconte, B. L. Chittari, K. Watanabe, T. Taniguchi, S. Adam, D. Graf, and C. R. Dean, Dynamic band-structure tuning of graphene moiré superlattices with pressure, Nature (London) **557**, 404 (2018).

[24] S. Pei, Z. Wang, and J. Xia, High pressure studies of 2D materials and heterostructures: A review, Mater. Design **213**, 110363 (2022).

[25] M. Yankowitz, S. Chen, H. Polshyn, Y. Zhang, K. Watanabe, T. Taniguchi, D. Graf, A. F. Young, and C. R. Dean, Tuning superconductivity in twisted bilayer graphene, Science **363**, 1059 (2019).

[26] S. Carr, S. Fang, P. Jarillo-Herrero, and E. Kaxiras, Pressure dependence of the magic twist angle in graphene superlattices, Phys. Rev. B **98**, 085144 (2018).

[27] B. L. Chittari, N. Leconte, S. Javvaji, and J. Jung, Pressure induced compression of flatbands in twisted bilayer graphene, Electron. Struct. **1**, 015001 (2018).

[28] L. Ge, K. Ni, X. Wu, Z. Fu, Y. Lu, and Y. Zhu, Emerging flat bands in large-angle twisted bi-layer graphene under pressure, Nanoscale **13**, 9264 (2021).

[29] A. Lopez-Bezanilla, Emergence of flat-band magnetism and half-metallicity in twisted bilayer graphene, Phys. Rev. Mater. **3**, 054003 (2019).

[30] F. Yndurain, Pressure-induced magnetism in rotated graphene bilayers, Phys. Rev. B **99**, 045423 (2019).

[31] M. Romanova and V. Vlček, Stochastic many-body calculations of moiré states in twisted bilayer graphene at high pressures, Npj Comput. Mater. **8**, 11 (2022).

[32] F. Sánchez-Ochoa, F. Hidalgo, M. Pruneda, and C. Noguez, Unfolding method for periodic twisted systems with commensurate moiré patterns, J. Phys.: Condens. Matter **32**, 025501 (2020).

[33] P. Ordejón, E. Artacho, and J. M. Soler, Self-consistent order-n density-functional calculations for very large systems, Phys. Rev. B **53**, R10441 (1996).

[34] J. M. Soler, E. Artacho, J. D. Gale, A. García, J. Junquera, P. Ordejón, and D. Sánchez-Portal, The siesta method for ab initio order-n materials simulation, J. Phys.: Condens. Matter **14**, 2745 (2002).

[35] J. P. Perdew, K. Burke, and M. Ernzerhof, Generalized Gradient Approximation Made Simple, Phys. Rev. Lett. **77**, 3865 (1996).

[36] N. Troullier and J. L. Martins, Efficient pseudopotentials for plane-wave calculations, Phys. Rev. B **43**, 1993 (1991).

[37] H. J. Monkhorst and J. D. Pack, Special points for brillouin-zone integrations, Phys. Rev. B **13**, 5188 (1976).

[38] K. Momma and F. Izumi, Vesta 3 for three-dimensional visualization of crystal, volumetric and morphology data, J. Appl. Crystallogr. **44**, 1272 (2011).

[39] V. H. Nguyen, T. X. Hoang, and J. Charlier, Electronic properties of twisted multilayer graphene, JPhys. Mater. **5**, 034003 (2022).

[40] F. D. Murnaghan, The compressibility of media under extreme pressures, Proc. Natl. Acad. Sci. U.S.A. **30**, 244 (1944).

[41] G. Yu, M. I. Katsnelson, and S. Yuan, Pressure and electric field dependence of quasicrystalline electronic states in $30°$ twisted bilayer graphene, Phys. Rev. B **102**, 045113 (2020).

[42] B. Padhi and P. W. Phillips, Pressure-induced metal-insulator transition in twisted bilayer graphene, Phys. Rev. B **99**, 205141 (2019).

[43] M. Hanfland, H. Beister, and K. Syassen, Graphite under pressure: Equation of state and first-order raman modes, Phys. Rev. B **39**, 12598 (1989).

[44] N. N. Nam and M. Koshino, Lattice relaxation and energy band modulation in twisted bilayer graphene, Phys. Rev. B **96**, 075311 (2017).

[45] N. P. Kazmierczak, M. Van Winkle, C. Ophus, K. C. Bustillo, S. Carr, H. G. Brown, J. Ciston, T. Taniguchi, K. Watanabe, and D. K. Bediako, Strain fields in twisted bilayer graphene, Nat. Mater. **20**, 956 (2021).

[46] M. M. van Wijk, A. Schuring, M. Katsnelson, and A. Fasolino, Relaxation of moiré patterns for slightly misaligned identical lattices: graphene on graphite, 2D Mater. **2**, 034010 (2015).

[47] F. Gargiulo and O. V. Yazyev, Structural and electronic transformation in low-angle twisted bilayer graphene, 2D Mater. **5**, 015019 (2017).

[48] H. Yoo, R. Engelke, S. Carr, S. Fang, K. Zhang, P. Cazeaux, S. H. Sung, R. Hovden, A. W. Tsen, T. Taniguchi *et al.*, Atomic and electronic reconstruction at the van der waals interface in twisted bilayer graphene, Nat. Mater. **18**, 448 (2019).

[49] V. H. Nguyen, D. Paszko, M. Lamparski, B. Van Troeye, V. Meunier, and J.-C. Charlier, Electronic localization in small-angle twisted bilayer graphene, 2D Mater. **8**, 035046 (2021).

[50] S. Zhu, J. A. Stroscio, and T. Li, Programmable Extreme Pseudomagnetic Fields in Graphene by a Uniaxial Stretch, Phys. Rev. Lett. **115**, 245501 (2015).

[51] M. A. Vozmediano, M. Katsnelson, and F. Guinea, Gauge fields in graphene, Phys. Rep. **496**, 109 (2010).

[52] D. Pesin and A. H. MacDonald, Spintronics and pseudospintronics in graphene and topological insulators, Nat. Mater. **11**, 409 (2012).

[53] D. V. Tuan, F. Ortmann, D. Soriano, S. O. Valenzuela, and S. Roche, Pseudospin-driven spin relaxation mechanism in graphene, Nat. Phys. **10**, 857 (2014).

[54] A. V. Rozhkov, A. Sboychakov, A. Rakhmanov, and F. Nori, Electronic properties of graphene-based bilayer systems, Phys. Rep. **648**, 1 (2016).

[55] E. McCann and M. Koshino, The electronic properties of bilayer graphene, Rep. Prog. Phys. **76**, 056503 (2013).

[56] G. E. Volovik, Exotic lifshitz transitions in topological materials, Phys. Usp. **61**, 89 (2018).

[57] S. Predin, P. Wenk, and J. Schliemann, Trigonal warping in bilayer graphene: Energy versus entanglement spectrum, Phys. Rev. B **93**, 115106 (2016).

[58] T. Zhang, C. Gao, D. Liu, Z. Li, H. Zhang, M. Zhu, Z. Zhang, P. Zhao, Y. Cheng, and W. Huang, Pressure tunable van hove singularities of twisted bilayer graphene, Nano Lett. **22**, 5841 (2022).

[59] A. G. Kvashnin, L. A. Chernozatonskii, B. I. Yakobson, and P. B. Sorokin, Phase diagram of quasi-two-dimensional carbon, from graphene to diamond, Nano Lett. **14**, 676 (2014).

[60] L. A. Chernozatonskii, V. A. Demin, and D. G. Kvashnin, Moiré diamones: New diamond-like films of semifunctionalized twisted graphene layers, J. Phys. Chem. Lett. **13**, 5399 (2022).

[61] P. B. Sorokin and B. I. Yakobson, Two-dimensional diamond-diamane: current state and further prospects, Nano Lett. **21**, 5475 (2021).

[62] F. Birch, Finite elastic strain of cubic crystals, Phys. Rev. **71**, 809 (1947).